



Article

Performance and Consistency of Final Global Ionospheric Maps from Different IGS Analysis Centers

Wei Li *, Keke Wang and Kaitian Yuan

School of Geography and Information Engineering, China University of Geosciences, Wuhan 430078, China
* Correspondence: weili@cug.edu.cn

Abstract: Ionospheric delay is one of the most problematic errors in satellite-based positioning data processing. The Global Ionospheric Map (GIM), which is publicly available daily in various analysis centers, is thus vitally important for positioning users. There are variations in the accuracy and consistency of GIMs issued by Ionosphere Associate Analysis Centers (IAACs) due to the differences in ionospheric modeling methods and selected tracking stations. In this study on the International GNSS Service's (IGS) final GIM, the ionospheric total electron content (TEC) (from 243 global navigation satellite system (GNSS) monitoring stations around the world) and the ionospheric TEC (from the Jason-3 altimeter satellite) are selected as reference. By using these three references, we evaluate the performance and consistency of final GIM products from seven IGS IAACs, including the Chinese Academy of Sciences (CAS), the Center for Orbit Determination in Europe (CODE), Natural Resources Canada (EMR), the European Space Agency (ESA), the Jet Propulsion Laboratory (JPL), Universitat Politècnica de Catalunya (UPC), and Wuhan University (WHU) in the mid-solar activity year (2022) and the low-solar activity year (2020). Firstly, the comparison with the IGS final GIM shows that the consistency of each GIMs is basically the same, with the mean value ranging from -0.3 TECu (total electron content unit) to 1.4 TECu. Secondly, the validation with Jason-3 altimeter satellite shows that the accuracy of several GIMs is almost the same, except for the JPL with the worst accuracy and an overall mean deviation (BIAS) between 2 and 6 TECu. Thirdly, the comparison with VTEC extracted from GNSS monitor stations shows that the CAS has the best accuracy in different latitude bands with a root mean square (RMS) of about 2.2–4.7 TECu. In addition, it is found that the accuracy in areas with more stations for ionospheric modelling is better than those with less stations in different latitude bands; meanwhile, the accuracy is closely related to the modeling methods of different GIMs.

Keywords: ionosphere; total electron content (TEC); global ionospheric maps (GIMs); Jason-3



Citation: Li, W.; Wang, K.; Yuan, K. Performance and Consistency of Final Global Ionospheric Maps from Different IGS Analysis Centers. *Remote Sens.* **2023**, *15*, 1010. <https://doi.org/10.3390/rs15041010>

Academic Editor: Michael E. Gorbunov

Received: 16 January 2023
Revised: 4 February 2023
Accepted: 8 February 2023
Published: 12 February 2023



Copyright: © 2023 by the authors. Licensee MDPI, Basel, Switzerland. This article is an open access article distributed under the terms and conditions of the Creative Commons Attribution (CC BY) license (<https://creativecommons.org/licenses/by/4.0/>).

1. Introduction

The ionosphere is distributed between 60 km and 2000 km above the earth's surface, which can cause time delays of several meters or even hundreds of meters [1]. It is one of the most important error sources in global navigation satellite system (GNSS) positioning, which seriously affects the accuracy and precision of satellite navigation positioning and timing. Compared with traditional ionospheric monitoring methods such as ionospheric drapes, high-power scattering radars, and laser radars, GNSS positioning has the advantages of low cost, high-precision, all-weather use, and global coverage, among other things. With the development of satellite systems such as the Global Positioning System (GPS), Globalnaya Navigatsionnaya Sputnikovaya Sistema (GLONASS), Galileo, as well as Bei-Dou Navigation Satellite System (BDS), ionospheric monitoring with GNSS positioning has become the most common and effective means for high-resolution ionospheric monitoring [2]. Therefore, the Global Ionospheric Map (GIM) product based on GNSS positioning is an important data resource for the global total electron content (TEC) research and application at present. The GIM can be used to invert the pattern of ionospheric variation as well

as to provide ionospheric delay correction in single-frequency navigation and positioning studies [3].

In 1998, the International GNSS Service (IGS) Ionosphere Associate Analysis Centers (IAACs) were established to publish three types of ionospheric products, i.e., the predicted GIM, the rapid GIM, and the final GIM [4]. There are seven institutions submitting official products to the IGS, with space resolutions of 2.5° and 5° in latitude and longitude, respectively, and time resolutions ranging from 0.5 to 2 h. The Center for Orbit Determination in Europe (CODE), the Jet Propulsion Laboratory (JPL) in the United States, the European Space Agency (ESA), and Universitat Politècnica de Catalunya (UPC) have provided products to the IGS Ionospheric Integration Center since 1998 [5–9]. Natural Resources Canada began submitting EMR products to the IGS in April 2015. The Chinese Academy of Sciences (CAS) and Wuhan University (WHU) have been officially offering their services since 2016. The IGS center evaluated the GIMs from some IAACs to provide its final product. Presently, the GIM products from different IAACs are basically classified into three types: predicted, rapid (less than 24 h delay), and final (11 days delay) [10], with the uniform IONEX format issued to the public [11]. Since 2020, the IGS final GIM changed from previous combinations of COD and JPL GIMs to a combination of COD, ESA, JPL, and UPC GIMs.

The differences in generating GIM products among different agencies include the mathematical models, the selected GNSS tracking stations, and the solving strategies, as shown in Table 1, which lead to differences in the accuracy of different types of GIM products produced by different institutions [12]. Spherical harmonic (SH) functions of order 15×15 are adopted by the CODE, ESA, EMR, and WHU to construct global ionospheric models, while the CAS combines the SH with generalized trigonometric series (GTS) functions. The UPC construct model, based on single stations using tomographic functions with splines, aims to build a global ionospheric TEC model using interpolation. In the case of the JPL, the global modeling is performed using a three-shell model [13]. The methods used for the JPL, CODE, ESA, and UPC have been extensively summarized by Li et al. [14].

Table 1. Processing strategy and products information of GIMs from each analysis center.

Agency	Method	Satellite Systems	GIMs Products	Time Resolution	
CAS	Spherical harmonic (SH) functions with generalized trigonometric series	Integrate the global and local models	G, C, R	rapid, final	0.5 h
COD	SH	Global modeling	G, R	predicted, rapid, final	1 h
EMR	SH	Global modeling	G, R	final	1 h
ESA	SH	Global modeling	G, R	predicted, rapid, final	2 h
UPC	Tomographic functions with Splines	Modeling based on single station	G	predicted, rapid, final	2 h
JPL	Three-shell model	Global modeling	G	rapid, final	2 h
WHU	SH	Global modeling	G, R	rapid, final	2 h

A systematic and intensive evaluation of the application effectiveness of different GIM products can provide the reference for ionospheric TEC detection, environmental monitoring, and ionospheric delay correction services for navigation users around the world. Regarding the evaluation of GIMs, there are two main independent external data sources that can be used (altimeter satellite and GNSS monitoring station data) [15–17]. Many scholars have carried out evaluation work with extensive accuracy on the application performance of different GIMs. For the construction of GIM, they have all used TEC data obtained from the distribution of worldwide GPS stations, which are inherently biased toward continents in the northern hemisphere, but very sparse in the Southern Hemisphere and over the entire ocean [18]. At the same time, some scholars are constantly studying ways to extract VTEC data from GNSS monitoring stations with greater accuracy [19]. To

solve the problem of the uneven distribution of GNSS tracking stations, Chen et al. [20] combined GNSS, altimeter satellite, radio occultation, and DORIS (Doppler Orbit and Radio position Integration by Satellite) data to build a multiple-source global ionospheric model. The accuracy and reliability of the GIMs generated using the combined data are significantly improved in the oceanic range. Ho et al. [21] compared GIMs with TOPEX/Poseidon and Bent climate models on a global scale as early as 1997, which confirmed the accuracy of GIMs in responding to global ionospheric features in near real time. Then, by drawing comparisons with TOPEX/Poseidon, Orus et al. [22] found that the performance of GIMs is better than IRI and Bent models, of which the global relative error driven from GPS data was less than 30% compared to TOPEX/Poseidon. Roma et al. [23] provide extensively models that are used to generate products for the different analysis centers and compare the models used with the three newly added analysis centers (CAS, WHU, and EMR) with the models of four traditional institutions. Luo et al. [24] evaluated the performance of various ionospheric models using JPL's GIMs TEC data as a reference. Nie et al. [25] evaluated the accuracy of real-time ionospheric products. Zhang et al. [13] compared and analyzed the product accuracy of the WHU Analysis Center with other institutions around the world since 2016. Jerez GO et al. [26] validated the product accuracy of GIMS on a global scale based on the critical frequency of the F2 layer measured directly in the ionosphere. Moreover, the ionosphere is formed by free electrons generated by solar radiation from neutral gas molecules in the Earth's atmosphere, so the variation of the ionosphere is closely related to solar activity. Jee et al. [18] analyzed the accuracy of CODE analysis center's products during 1998–2009 with TOPEX/Jason altimeter satellites. Li et al. [27] evaluated the overall performance of five final GIMs, including the CODE, JPL, ESA, CAS, and UPC, during two solar cycles from 1998 to 2015. The ionospheric activity has significant regional characteristics, and ionospheric equatorial anomalies exist at low latitudes. Zhang et al. [28] investigate the differences between four ionospheric data sources (ionosonde, IGS, TOPEX/Poseidon, and IRI2001) at low-latitude stations in Hainan. Xue et al. [29] and Lai et al. [30] evaluated the accuracy of CODE's GIM over China. Xiang et al. [31] intensively discussed the accuracy of different GIMs in the China. Wang et al. [32] analyzed the accuracy of GIMs at mid-latitudes and low latitudes in China.

Based on the studies of these scholars, there is still a lack of research on the final products covering all IAACs around the world. Therefore, this paper presents the comprehensive evaluation of seven IAAC final GIM products by drawing comparisons with three references, including IGS final GIMs, Jason-3 altimeter satellite-based solutions, and TEC from GNSS monitoring stations. In the experiment, the evaluation is firstly implemented on a global scale, and then the global area is divided into six parts of low, mid, and high latitudes in the Northern and Southern Hemispheres for sub-regional accuracy assessment. The research can provide precision support for the ionospheric delay correction in single-frequency navigation and positioning. At the same time, it can also provide a reference for users in selecting the GIM that best fits their research area.

The paper is organized as follows. After the brief introduction in Section 1, the mathematical models used for extracting vertical total electron content (VTEC) from ionospheric products and evaluation methods are introduced in Section 2. In Section 3, a comprehensive evaluation of seven different final GIM products from IAACs are analyzed in different solar activity years, where the reference ionospheric VTEC derives from IGS GIMs, GNSS monitoring stations, and Jason-3 altimeter satellites. Finally, a discussion is given in Section 4 and conclusions are drawn in Section 5.

2. Methodology

In this section, to examine the performance and reliability of these seven GIMs, the mathematical model is applied as follows. In the evaluation process, binary spatial interpolation with linear temporal interpolation of the grid data is required in order to calculate the VTEC value at any location in time, as shown in Section 2.1. The method of drawing comparisons with the IGS final GIM is presented in Section 2.2. Next, VTEC extraction

using Jason-3 altimetry satellite is investigated in Section 2.3. Then, the VTEC extraction process from dual-frequency GNSS observations of monitoring station is presented in Section 2.4. The statistics index used in the evaluation process is given in Section 2.5.

2.1. VTEC Interpolation

In practice, the grid data with a time resolution of 2 h and a spatial resolution of $5^\circ \times 2.5^\circ$ need to be interpolated to obtain the VTEC at the ionospheric pierce points of different epoch acquired by GNSS monitoring stations and Jason-3 altimeter satellites, as shown in Equation (1).

$$VTEC(x, y) = \sum_{i=1}^4 \left(\frac{\sqrt{(x_i-x)^2+(y_i-y)^2}}{\sum_{k=1}^4 \sqrt{(x_k-x)^2+(y_k-y)^2}} \times V_i \right) \quad (1)$$

$$VTEC(t) = \frac{t-t_{min}}{7200} * V_{t_{max}} + \frac{t_{max}-t}{7200} * V_{t_{min}}$$

where $VTEC(x, y)$ and $VTEC(t)$ are the VTEC values at the desired coordinate and epoch, respectively; x_i, y_i, x_k, y_k is the coordinates of the four grid points; $V_i (i = 1, 2, 3, 4)$ is the VTEC value on the four grid points; t_{max} and t_{min} are the two closest epoch values at the desired epoch; $V_{t_{max}}$ and $V_{t_{min}}$ are the VTEC values for the two closest epoch at the desired epoch values, respectively.

2.2. Consistency with the IGS Final GIM

The spatial resolutions of different GIMs are consistent, but there are some differences in their time resolutions, which should be unified in the comparison. There are three types of time resolutions among the following products: 0.5 h, 1 h, and 2 h. The time resolutions of 2 h are selected as reference, and then the data with time intervals of 0.5 h and 1 h are extracted and combined according to the reference time. Additionally, for the consistency evaluation, the kernel density estimation of the difference between IAAC GIMs and IGS final GIMs is performed, as shown in Equation (2).

$$g(x) = \frac{1}{\sqrt{2\pi}} e^{-\frac{x^2}{2}}$$

$$f(x) = \frac{1}{nh} \sum_{j=1}^n g\left(\frac{x-x_j}{h}\right) \quad (2)$$

where n is the number of data and h is the smoothing parameter, also called the bandwidth.

2.3. Validation with Jason-3 Satellite

Altimeter satellites provide ionospheric data with the widest coverage and longest continuous observation time independent of GNSS positioning. The orbital altitude of Jason-3 satellite is $1336 \text{ km} \times 1336 \text{ km}$, with an orbital inclination of 66 degrees. Furthermore, the orbital period of Jason-3 is 9.961 days. Dual frequencies in the C-band and Ku-band signals are transmitted by Jason-3 to the ocean surface which enables ionospheric TEC inversion in the signal propagation path [33]. Therefore, altimeter satellites can be considered as an independent source of TEC data. The comparison with Jason-3-based solutions can verify the external accuracy, and the calculation formula is shown in Equation (3).

$$VTEC = iono_{jason3} \times \frac{f^2}{40.3} \quad (3)$$

where $iono_{jason3}$ is the Ku-band ionospheric range correction in meters; f is the frequency of the Ku band, which is 13.575 GHz.

2.4. Validation with GNSS Monitoring Stations

The ionospheric data extracted from GNSS monitoring stations can be used to verify the internal accuracy of GIMs. The slant TEC (STEC) along the radio propagation path

can be obtained from the dual-frequency carrier phase observations and the pseudorange observations [34]. Then, VTEC at the ionospheric puncture point (IPP) can be obtained using the differential code deviation (DCB) correction and mapping function [35]. It is important to note that the satellite DCB and receiver DCB are assumed to a daily number in this process. Although Zhang et al. [36,37] confirmed a subtle variation in the receiver DCB on an intra-day scale, the effect of the intra-day variation in the DCB on the accuracy of GIM generation can be negligible with the present experience. The process of VTEC extraction using dual-frequency observations can be divided into four steps, outlined below.

The first step is the pre-processing of data from GNSS stations. We use M-W linear combination to detect the cycle slips and gross errors shown in Equation (4).

$$\begin{aligned} L_6 &= \frac{c}{f_1 - f_2} (f_1 L_1 - f_2 L_2) - \frac{1}{f_1 + f_2} (f_1 P_1 + f_2 P_2) \\ N_w &= \frac{L_6}{(f_1 - f_2)} = (f_1 L_1 - f_2 L_2) - \frac{f_1 - f_2}{f_1 + f_2} \left(\frac{P_1}{\lambda_1} + \frac{P_2}{\lambda_2} \right) = N_1 - N_2 \end{aligned} \quad (4)$$

$$\begin{aligned} \overline{N_\omega^i} &= \overline{N_\omega^{i-1}} + \frac{1}{i} (N_\omega^i - N_\omega^{i-1}) \\ \sigma_i^2 &= \sigma_{i-1}^2 - \frac{1}{i} \left[\left(N_\omega^i - \overline{N_\omega^{i-1}} \right)^2 - \sigma_{i-1}^2 \right] \end{aligned} \quad (5)$$

where L_6 is the combined M-W phase observation; f_1 and f_2 are the values at the first and second frequency, respectively; L_1 and L_2 are the carrier phase observations; N_w is the modality of the ambiguous combination of the wide-lane carrier phase observations; N_1 and N_2 are the ambiguities on L_1 and L_2 , respectively. Meanwhile, N_ω and its mean $\overline{N_\omega}$ are applied to make a judgment about the existence of cycle slips. If $\left| N_\omega^i - \overline{N_\omega^{i-1}} \right|$ is larger than $4\sigma_i$ and $\left| N_\omega^{i+1} - N_\omega^i \right|$ is less than 1, cycle slips exist. If cycle slips exist, they can be determined and resolved by a linear combination independent of geometry, as shown in Equation (6). Finally, the gross errors detected in the M-W linear combination is removed using the ionosphere-free combination shown in Equation (7).

$$L_4 = L_1 - L_2 \quad (6)$$

$$\begin{aligned} L_3 &= \frac{1}{f_1^2 - f_2^2} (f_1^2 L_1 - f_2^2 L_2) \\ P_3 &= \frac{1}{f_1^2 - f_2^2} (f_1^2 P_1 - f_2^2 P_2) \end{aligned} \quad (7)$$

where L_4 is the geometry-free combined observation; L_3 and P_3 are the ionosphere-free combined observations of the phase and the code, respectively.

The second step involves smoothing pseudorange using the carrier, as presented in Equations (8) and (9), and the noise effects are also alleviated in this processing.

$$\begin{aligned} P_4 &= P_{1,j}^i - P_{2,j}^i = d_{ion,1,j}^i - d_{ion,2,j}^i + cDCB^i + cDCB_j \\ L_4 &= L_{1,j}^i - L_{2,j}^i = - \left(d_{ion,1,j}^i - d_{ion,2,j}^i \right) - \lambda \left(b_{1,j}^i - b_{2,j}^i \right) - \lambda \left(N_{1,j}^i - N_{2,j}^i \right) \end{aligned} \quad (8)$$

$$\begin{aligned} P_{4,sm}(t) &= \omega_t P_4(t) + (1 - \omega_t) P_{4,prd}(t) \\ P_{4,prd}(t) &= P_{4,sm}(t-1) + [L_4(t) - L_4(t-1)] \end{aligned} \quad (9)$$

where DCB^i and DCB_j are the differential code biases of the satellite and the receiver; t means the number of epochs; ω_t is the weighting factor associated with the epoch, $\omega_t = 1$, when $t = 1$; b is the satellite and receiver instrument phase biases; N is the ambiguity of the carrier phase. The third step is to extract the STEC value at IPP. The ionospheric delay can be expressed, as shown in Equation (10). After substituting it into Equation (8), we can obtain the formula for STEC at IPP, as shown in Equation (11).

$$d_{ion} = \frac{40.3}{f^2} STEC \quad (10)$$

$$P_{4,sm} = 40.3 \left(\frac{1}{f_1^2} - \frac{1}{f_2^2} \right) STEC + cDCB^i + cDCB_j \quad (11)$$

The fourth step is to calculate the VTEC value at IPP using the mapping function. The VTEC values of the IPP at different epochs can be obtained by Equation (12).

$$VTEC = \cos \left(\arcsin \left(\frac{R}{R+H} \sin(\alpha z) \right) \right) \left[-\frac{f_1^2 f_2^2}{40.3(f_1^2 - f_2^2)} (P_{4,sm} - cDCB_j - cDCB^i) \right] \quad (12)$$

where the receiver and satellite *DCB* are corrected by the *DCB* products from the CAS in this research; *z* is the satellite zenith distance; *R* is the mean radius of the earth; and *H* is the height of the ionosphere. The satellite cut-off elevation angle is set at 15 degrees.

2.5. Index of Precision

On a global scale, the intensity of solar radiation, geomagnetic field, physical composition, and the density of the atmosphere vary from different geographical locations. As a result, the ionospheric electron density is not uniformly distributed in space, and the different latitudinal bands exhibit different space properties. The ionospheric activity is more active at low latitudes, and equatorial anomalies with a double-hump structure exist near the magnetic equator at 18° north and south latitude. The mid-latitude ionosphere is relatively quiet, showing significant climatological characteristics such as solar cycles, seasons, and diurnal variations during the day. However, there is a minimum value at night near a 50° magnetic latitude. In the high latitudes, the diurnal variation is small and the seasonal variation is not obvious, but irregular changes such as ionospheric disturbances often occur near the polar region. Therefore, when conducting the accuracy assessment of different GIMs on a global scale, it is divided into six parts of low-, middle-, and high-latitude bands in the Northern and Southern Hemispheres for sub-regional assessment, where the low-, mid-, and high-latitude bands are in the ranges of (0° to 30°), (30° to 60°), and (60° to 90°).

The mean deviation (bias), standard deviation (STD), root mean square (RMS), and relative error (PER) between the different GIMs and the references are computed as indicators for the accuracy analysis, as shown in Equation (13).

$$\begin{aligned} bias &= \frac{\sum_{i=1}^N (TEC_{model}^i - TEC_{ref}^i)}{N} \\ STD &= \sqrt{\frac{\sum_{i=1}^N (TEC_{model}^i - TEC_{ref}^i - bias)^2}{N-1}} \\ RMS &= \sqrt{\frac{\sum_{i=1}^N (TEC_{model}^i - TEC_{ref}^i)^2}{N}} \\ PER &= \frac{\sum_{i=1}^N (|TEC_{model}^i - TEC_{ref}^i| / TEC_{ref}^i)}{N} \times 100\% \end{aligned} \quad (13)$$

The TEC_{model}^i and TEC_{ref}^i represent the VTEC from different IAAC GIMs and the chosen reference in the same location at one epoch, where *N* is the number of datasets. Then, the statistics are computed in Equation (13) for the selected latitude scale over one day.

3. Datasets and Experiments

In this section, the experimental dataset and processing strategy are first introduced. Then, the consistency is verified by comparing with the IGS-weighted final GIMs. Later, the external reliability of the different GIMs is verified by drawing comparisons with the VTEC extracted from the Jason-3 altimeter satellite. Finally, the internal reliability of different GIMs is verified by comparing with the VTEC values obtained from dual-frequency GNSS observations.

3.1. Datasets

The datasets of seven IAAC GIM products used for performance evaluation are taken from the Crustal Dynamics Data Information System (CDDIS) and the National Centers for Environmental Information. In order to comprehensively evaluate the performance and consistency of GIMs from different IAACs, data under different solar activity level conditions are selected. Figure 1 shows the sunspot number variation from 2017 to the present, where higher sunspot numbers are associated with more intense solar activity. Since the CAS and WHU formally submitted their products to the IGS Center in 2017, the years of 2020 and 2022 are selected for comparative analysis under different solar activity levels.

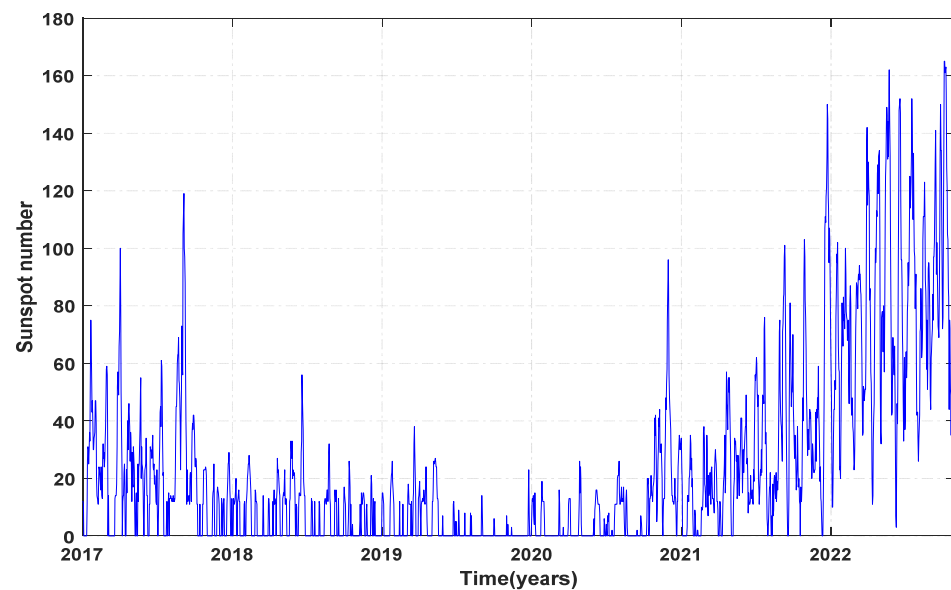


Figure 1. Sunspot number changes from 2017 to present.

Meanwhile, 243 GNSS monitoring stations distributed around the world are selected for evaluation, and their distributions are shown in Figure 2. Since different reference stations are used by different IAACs for GIM generation, the 243 monitoring stations used for the assessment might not be totally different from the reference stations used for the GIM generation, as some stations are the same. Then, the VTEC values are extracted based on the GNSS observation of these monitoring stations.

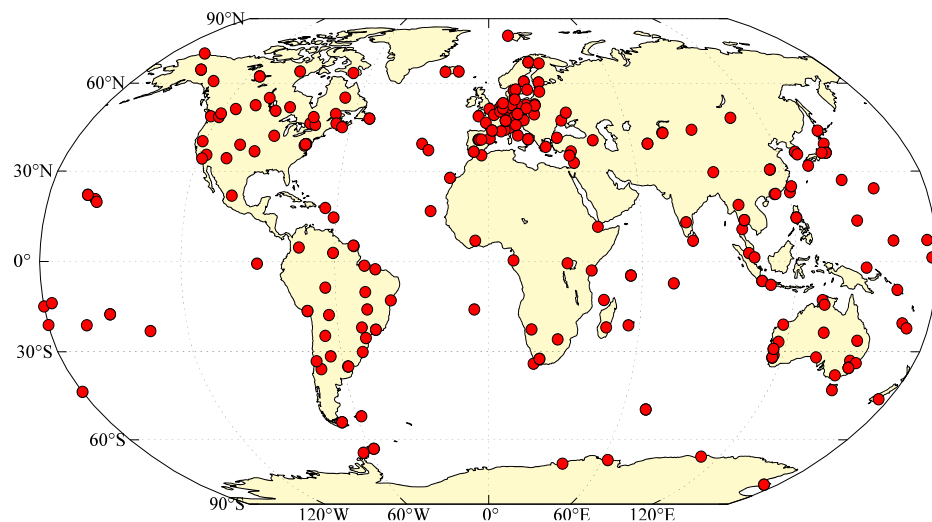


Figure 2. Distribution map of GNSS monitoring stations.

3.2. Consistency with IGS Final GIM

The low solar activity year (2020) and the mid solar activity year (2022) DOY 1 to DOY 267 are chosen to assess the consistency of different GIMs with the IGS final GIM. Since the research starts in October 2022, the up-to-date dataset until the end of September 2022 is selected in the experiments. The time resolutions of the three analysis centers (GIMs of the CAS, COD, and EMR) are 0.5 h, 1 h, and 1 h, respectively, while the time resolution of 2 h is chosen for the other centers. Therefore, the time resolutions of the CAS, COD, and EMR declined to 2 h. The STD, bias, RMS, and PER values of the VTEC differences between different GIMs and IGS final GIM in 2020 and 2022 are calculated according to Equation (13), with the time series statistics showing in Figure 3. Time series for 2020 are shown on the left side of the dashed line, and for 2022 on the right side. The yearly mean statistics are presented in Table 2.

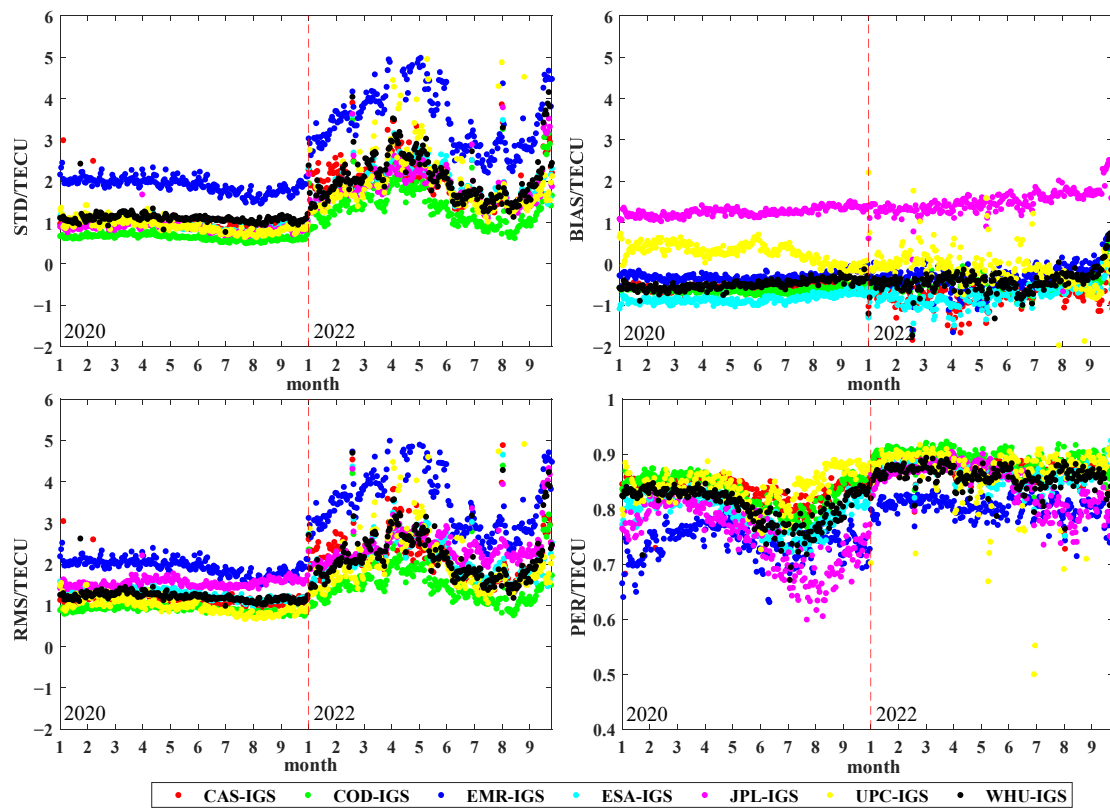


Figure 3. Model deviations of GIMs in 2020 and 2022 compared to the IGS final GIM.

Table 2. Annual average precision of ionospheric TEC for GIMs, in the units of TECu.

Error	Year	CAS-IGS	COD-IGS	EMR-IGS	ESA-IGS	JPL-IGS	UPC-IGS	WHU-IGS
STD	2020	0.984	0.641	1.907	0.930	0.880	0.916	1.101
	2022	2.004	1.391	3.465	1.935	1.864	2.002	2.097
Bias	2020	−0.582	−0.629	−0.305	−0.850	1.258	0.275	−0.499
	2022	−0.766	−0.495	−0.317	−0.762	1.487	−0.114	−0.431
RMS	2020	1.151	0.902	1.941	1.267	1.543	0.981	1.217
	2022	2.176	1.515	3.473	2.119	2.427	2.034	2.178
PER	2020	0.835	0.832	0.738	0.791	0.749	0.841	0.805
	2022	0.873	0.893	0.802	0.865	0.845	0.863	0.859

It is observed that the accuracy of different GIMs in the low solar activity year (2020) and the mid solar activity year (2022) has no much difference. As a whole, the accuracy of different GIMs is worse in mid-solar activity years than in low solar activity years, and

their RMS values are 1.286 TECu (total electron content unit) and 2.346 TECu, respectively. Meanwhile, considering the IGS final GIM as the reference, the correction effect is better in low solar activity years than in middle solar activity years, with the correction percentages of 79.9% and 85.7%, respectively. The maximum and minimum biases derive from the JPL and EMR during both low and mid solar activity years. Except for the JPL, the bias of all other GIMs is less than 1 TECu. In terms of global conformity to the IGS final GIM, the UPC is best in low solar activity years and the COD is best in mid solar activity years. Meanwhile, the EMR is the worst in both years, while the overall result can reach more than 80%. The difference in results is mainly due to the fact that the IGS final GIM is composed of different GIMs with combined weighting.

Kernel density estimation is used in probability theory to estimate unknown density functions, and is one of the nonparametric test methods, which only needs the input data and bandwidth to estimate the probability density function of the variable. This approach can also more effectively show the distribution of model bias between different GIMs and the IGS final GIM. We can observe the consistency of different GIMs with the IGS final GIM through the bias and STD of the curve. The kernel density estimation of different GIMs from the IGS final GIM is plotted, as shown in Figure 4. It can be found that the deviation distribution of GIMs (2020) from the IGS final GIM is more centralized in low solar activity years than in medium solar activity years (2022), while the COD is most consistent with the IGS final GIM and EMR is the worst. The STD values of the COD in low and high solar activity years are 0.064 TECu and 0.277 TECu, while those of UPC are 0.223 TECu and 1.02 TECu. For the effect of solar activity, the least effect is observed for WHU with STD values of 0.106 TECu and 0.303 TECu.

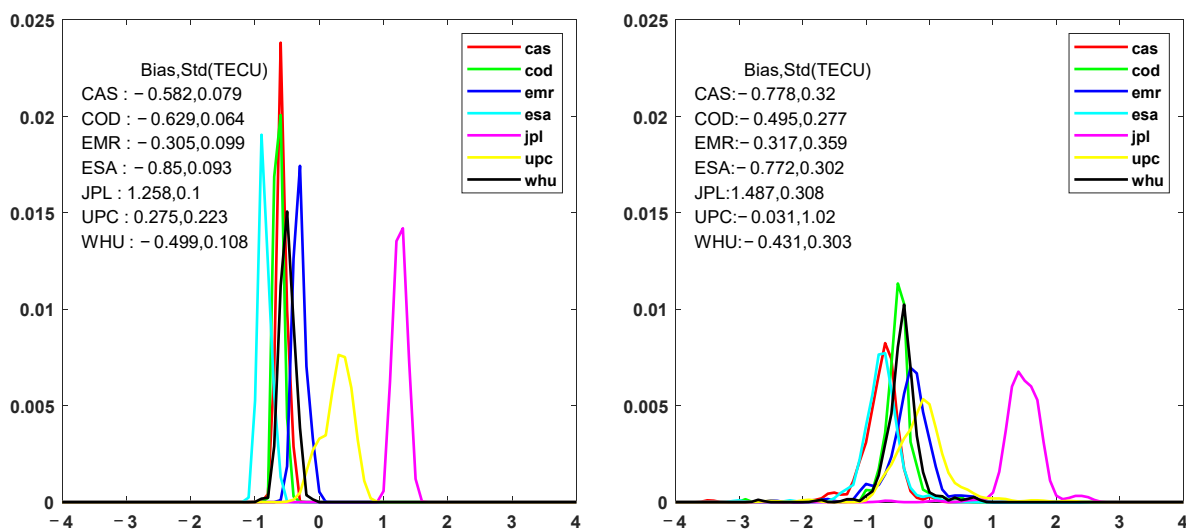


Figure 4. Kernel density estimation curves for different GIMs model deviations.

Considering the different level of ionospheric activity at different latitudes, the region from -85°S to 85°N is divided into six latitude bands, as shown in Section 2.5. The accuracy of GIMs in each latitude band is shown as Figure 5, where N and S represent the Northern and Southern Hemispheres, respectively; H, M, and L represent the high, mid, and low-latitude bands. It can be found that different GIMs demonstrate different performance levels among the latitude bands. The results show that the RMS values of high, middle, and low latitudes in the Northern and Southern Hemispheres are 1.751 TECu, 1.755 TECu, and 1.912 TECu and 0.964 TECu, 1.152 TECu, and 2.054 TECu, respectively. It is observed that the consistency of different GIMs with the IGS final GIM is best in the high-latitude band and worst in the low-latitude band, regardless of the solar activity level. This is mainly caused by the presence of equatorial anomalies in the ionosphere of the low-latitude band and the mid-latitude band. Meanwhile, the RMS values in the Northern Hemisphere and

Southern Hemisphere are 1.463 TECu and 1.127 TECu in 2020, compared to 2.138 TECu and 1.653 TECu in 2022. It is noticeable that the consistency is higher in the Northern Hemisphere than in the southern hemisphere. This is mainly due to the fact that the GIMs are generated based on global GNSS monitoring station data, which are more densely distributed in the Northern Hemisphere than in the Southern Hemisphere. Moreover, it could also be related to the concentration of anomalies and irregularities in the south due to the deviation of the geomagnetic equator. The EMR has the worst consistency and the COD has the best consistency between different GIMs and the IGS final GIM during low and mid solar activity years in different latitudinal bands, with similar results from other institutions. It is noteworthy that the performance of different GIMs in the low-latitude band in the mid-solar activity year shows three distinct groups, with the worst performance in EMR, whose RMS reaches 4.704 TECu, and the best performance in COD, whose RMS is 1.298 TECu. The RMS values of the other GIMs range from 2.108 TECu to 2.798 TECu. This indicates that the difference between different GIMs and IGS final GIMs with solar activity is mainly in the low-latitude band.

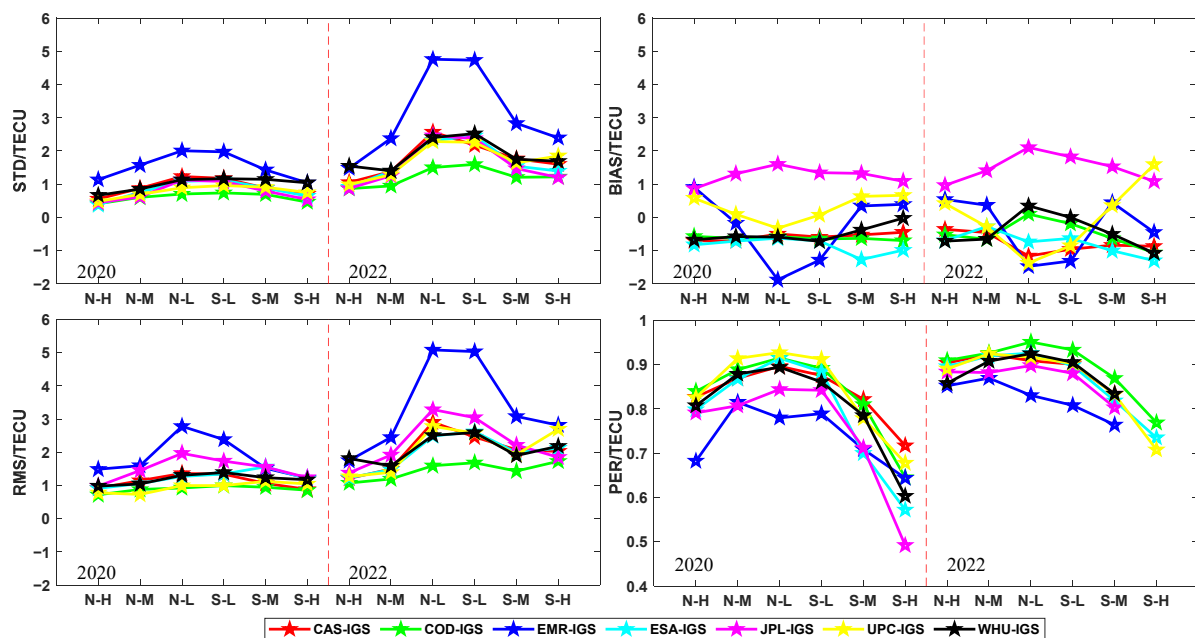


Figure 5. Model deviations of the GIMs compared to the IGS integrated GIM at different latitudinal bands.

3.3. Validation with Jason-3 VTEC

For the vast ocean area, the VTEC from sea level to the altitude of the altimetry satellite is extracted from the satellite altimetry data. The time resolution of the Jason-3-based VTEC values is 1 s, while the time resolution of the GIMs is 2 h. In this research, the time resolution is unified to 1 min during the processing. It is important to note that the altimetry satellite can only measure the ionospheric electron density below the altitude of the altimetry satellite orbit. There are systematic deviations between the VTEC extracted by Jason-3 altimetry satellite and the VTEC from the GIM, ranging from 2 to 5 TECu. Since there are data missing of Jason-3-based VTEC products for about two months during the experiment period, for the sake of fair comparison to avoid data gap, continuous datasets from DOY1 to DOY164 in 2020 and 2022 are selected for evaluation. The time series of the difference in VTEC between Jason-3-based solutions and different IAAC GIMs is shown in Figure 6, with the accuracy statistics presented in Table 3.

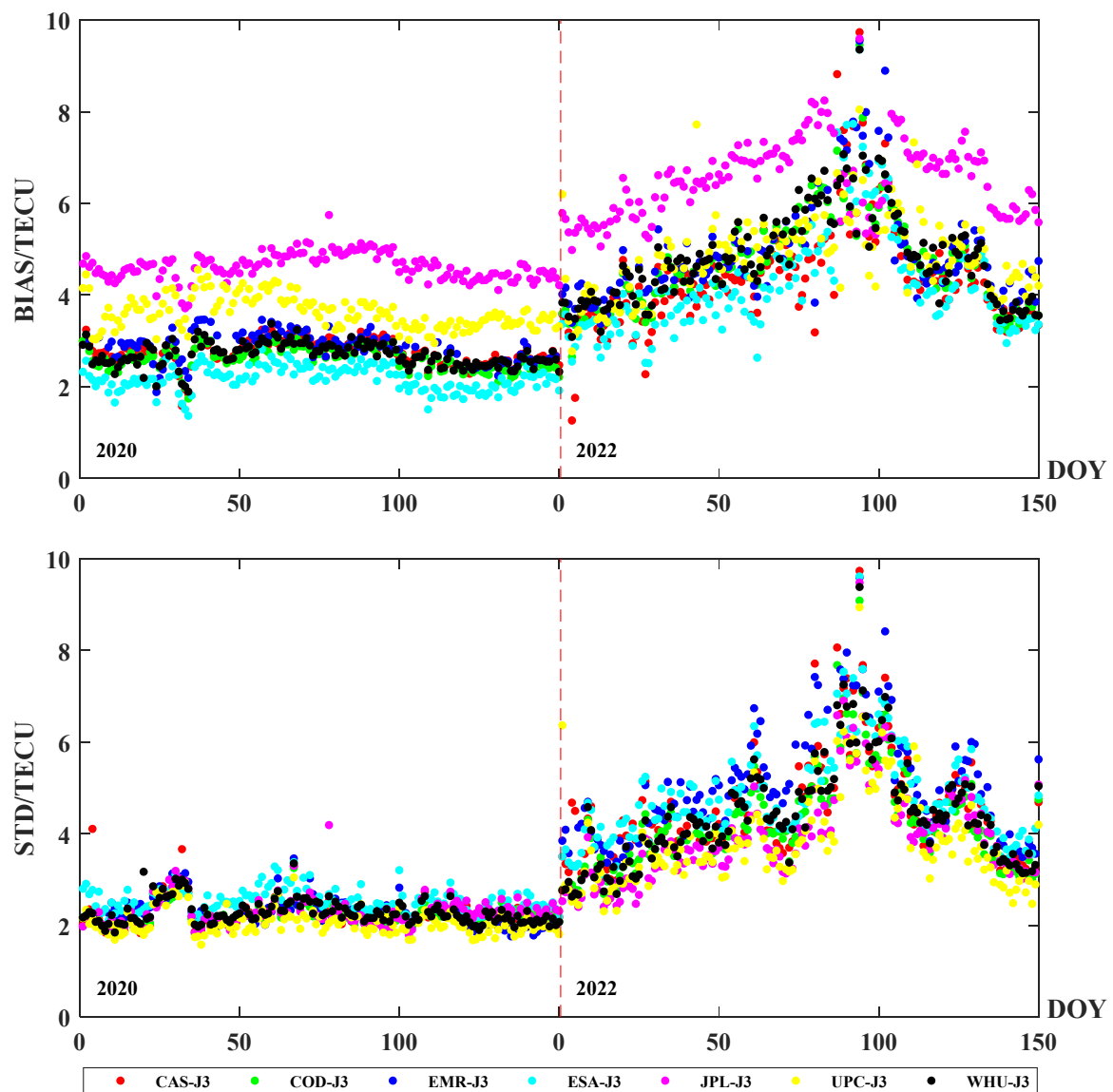


Figure 6. Time series figure of bias and STD of GIMs and Jason-3 altimeter satellite.

Table 3. Accuracy statistics of GIM versus Jason3 for different institutions in the units of TECu.

Error	Year	CAS-JA3	COD-JA3	EMR-JA3	ESA-JA3	JPL-JA3	UPC-JA3	WHU-JA3
RMS	2020	3.567	3.444	3.705	3.351	5.168	4.186	3.538
	2022	6.049	6.078	6.765	6.138	7.494	6.241	6.278
STD	2020	2.270	2.237	2.316	2.544	2.309	2.075	2.285
	2022	4.537	4.248	5.049	4.825	3.946	4.078	4.388
Bias	2020	2.735	2.609	2.877	2.171	4.615	3.626	2.691
	2022	3.692	4.139	4.291	3.553	6.212	4.453	4.271

According to the graphs, it can be found that the STD and bias between Jason-3 altimeter satellites and different GIMs in 2020 are overall less than those in 2022. The results show that the systematic VTEC deviations are more than 1 TECu between each GIM of different agencies and the Jason-3 altimeter satellite, which is consistent with the fact that the altimeter satellite observations do not include the ionospheric TEC from the altimeter satellite orbit altitude to the GNSS satellite orbit altitude. The differences are significantly larger in the middle years of solar activity compared to the low years, for which the mean bias and STD values are 4.373 TECu and 3.046 TECu compared to 4.439 TECu

and 2.291 TECu, respectively. The largest bias is found at the JPL among the seven IAACs with the annual average value of 5.413 TECu, while the bias among the other agencies ranges from 2.862 TECu to 4.040 TECu. In terms of the RMS index, the ESA is best in low solar activity years, and the CAS is best in mid solar activity years, which is not much different from the COD, ESA, and UPC. The results show that the JPL has significantly lower accuracy than the others at both mid and low solar activity years. Among the bias from Jason-3, the EMR has the most significant effect by solar activity. It should be noticed that the accuracy levels of the JPL and UPC are worse than the others. The mean RMS values of the JPL and UPC are 6.331 TECu and 5.214 TECu, respectively, with a mean RMS of about 4.871 TECu for the other five products. Meanwhile, the differences between 2020 and 2022 for seven GIMs are all about 2.5 TECu. Considering that the modeling methods used by the JPL and UPC are different from those used by the other five GIMs, it can be concluded that differences between GIM and Jason-3 in the marine area depend on differences in modeling methods. At the same time, the accuracy of different GIMs is independent of the solar activity level.

To more comprehensively analyze the accuracy of different GIMs in different latitude bands over the ocean, overlaying plots for the daily errors during the selected periods in 2020 and 2022 are shown in Figures 7 and 8. The ocean area is covered, and the magnitude of bias is presented in different colors where stronger differences are represented by redder colors. Table 4 shows the RMS statistics between different GIMs (VTEC data and Jason-3 data). The results show that the VTEC deviation distribution between different GIMs and Jason-3 altimetric satellite data has the worst accuracy at low latitudes and the best accuracy at high latitudes in general. It can also be found that the overall accuracy of the Southern Hemisphere is higher than that of the northern hemisphere. The main reason is that ocean areas are mainly located in the southern hemisphere, so Jason-3 satellites, which only acquire data over the ocean, can acquire more data from the Southern Hemisphere than from the northern hemisphere. Therefore, the accuracy in the Southern Hemisphere is slightly higher compared to the northern hemisphere. In the solar activity mid-year, the JPL has the same worst accuracy in the low- and mid-latitude bands; however, the high-latitude band differs somewhat. The accuracy of the EMR is the worst in the Northern Hemisphere high-latitude band, the accuracy of UPC is the worst in the Southern Hemisphere high-latitude band, while the WHU has the highest accuracy in the high-latitude band. The COD and CAS have the highest precision in the mid-latitude and low-latitude bands, respectively.

Table 4. RMS values of different GIMs in 2020 and 2022 relative to Jason3 in different latitudinal bands, in the units of TECu.

Latitude	Year	CAS-JA3	COD-JA3	EMR-JA3	ESA-JA3	JPL-JA3	UPC-JA3	WHU-JA3
N-H	2020	1.614	1.672	3.264	1.569	2.812	2.666	1.662
	2022	3.933	3.319	4.801	3.531	4.606	4.421	3.117
N-M	2020	3.511	3.491	3.854	3.214	5.253	3.989	3.549
	2022	5.332	5.004	6.163	5.256	6.684	5.082	5.181
N-L	2020	4.807	4.595	3.969	4.670	6.710	4.967	4.595
	2022	7.088	8.094	8.127	7.983	9.782	7.143	8.465
S-L	2020	4.125	3.946	3.754	4.078	5.758	4.633	3.990
	2022	7.146	7.523	7.836	7.776	8.994	7.157	7.828
S-M	2020	2.661	2.640	3.460	2.240	4.173	3.687	2.867
	2022	4.682	4.561	5.764	4.562	5.901	5.467	4.708
S-H	2020	2.066	1.975	3.163	1.743	3.329	3.236	2.240
	2022	4.173	3.918	5.035	3.769	4.896	5.585	3.756

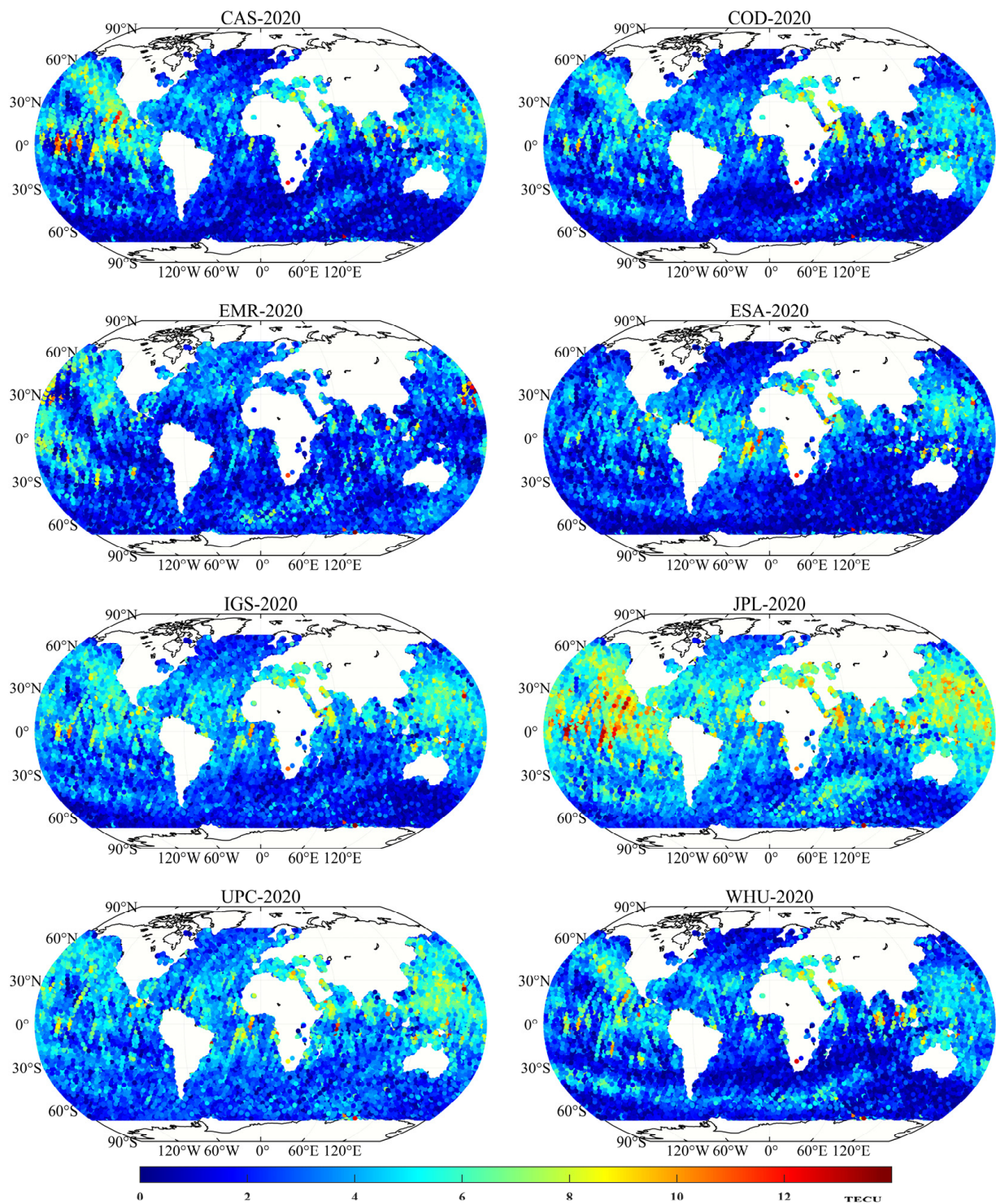


Figure 7. Bias distribution of different GIMs with Jason-3 altimetry satellites in 2020.

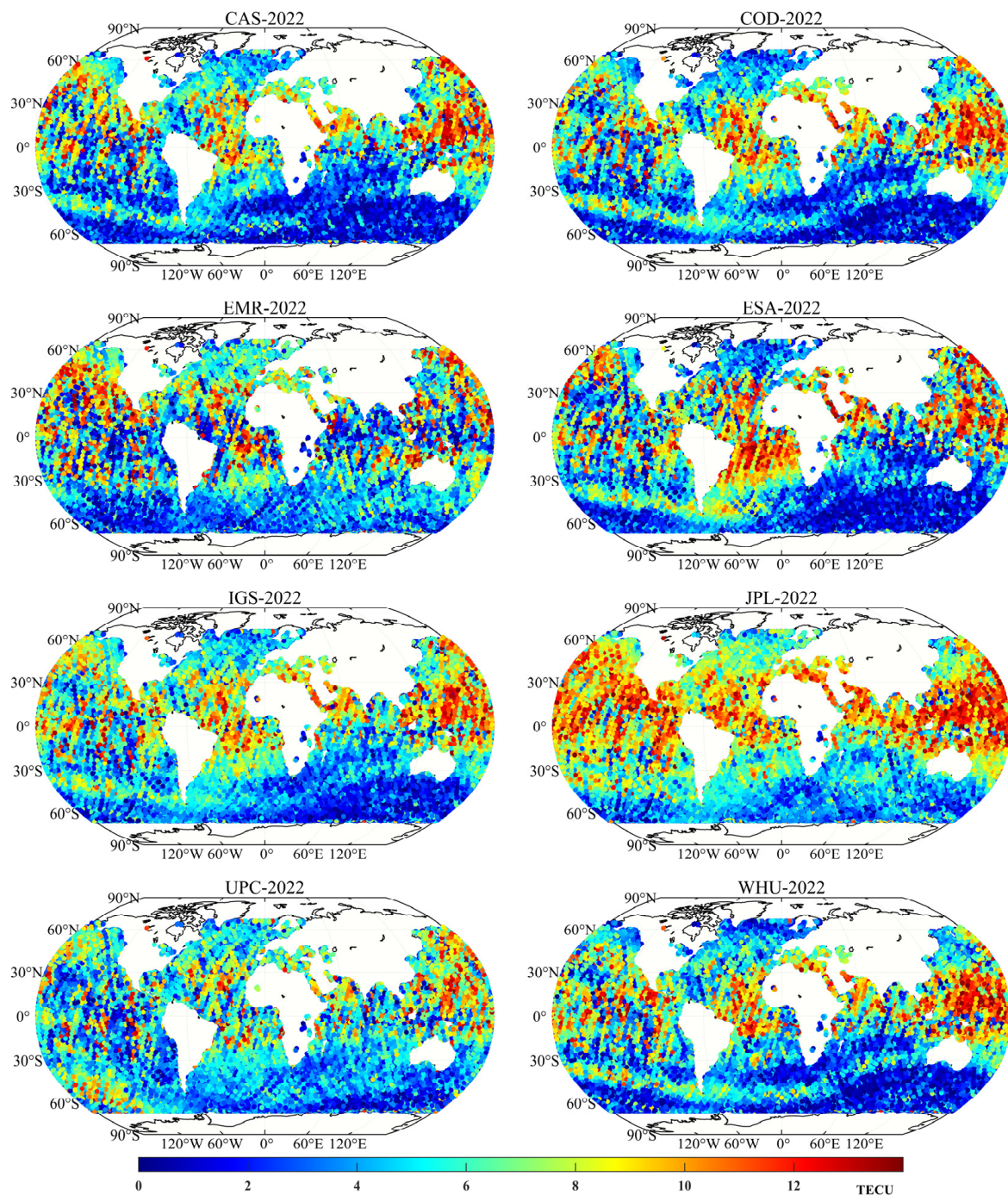


Figure 8. Bias distribution of different GIMs with Jason-3 altimetry satellites in 2022.

3.4. Validation with VTEC from Monitoring Stations

By calculating the RMS and bias values from the daily difference among all stations, time-series plots of the VTEC difference between IGS IAAC GIMs and the VTEC from GNSS monitoring stations are shown in Figure 9, where the null value is due to the missing ionospheric file. The corresponding accuracy statistics are given in Table 5, where the STA stands for the ionospheric VTEC extracted from monitoring stations.

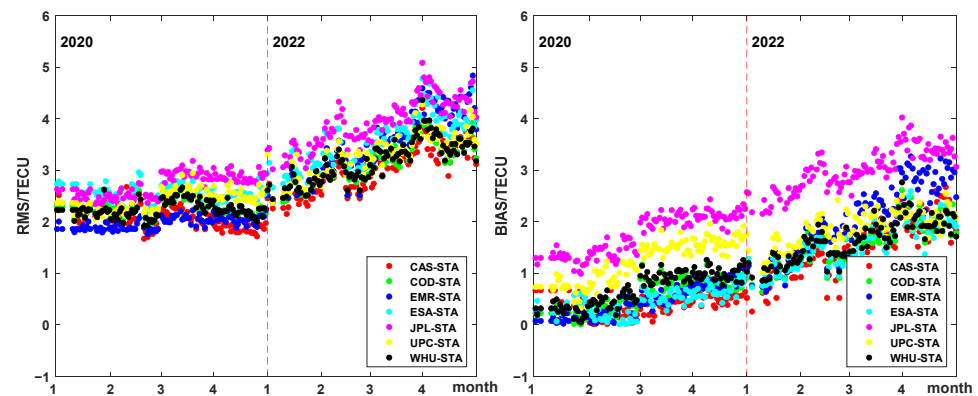


Figure 9. Time series plot of RMS and bias of GIMs with GNSS monitoring stations.

Table 5. Accuracy statistics of the difference between GIMs and GNSS monitoring stations, in the units of TECu.

Error	Year	CAS-STA	COD-STA	EMR-STA	ESA-STA	JPL-STA	UPC-STA	WHU-STA
RMS	2020	2.015	2.312	2.572	2.388	2.816	2.488	2.312
	2022	3.095	3.224	3.586	3.239	4.019	3.348	3.248
STD	2020	1.439	1.575	1.638	1.752	1.531	1.555	1.575
	2022	2.153	2.237	2.388	2.580	2.159	2.303	2.254
bias	2020	0.485	0.674	1.564	0.525	1.880	1.339	0.798
	2022	1.603	1.654	2.129	1.628	3.091	1.934	1.710

In terms of RMS and bias, the JPL has the lowest accuracy and the CAS has the highest accuracy in both low and mid solar activity years, with mean RMS values of 3.418 TECu and 2.555 TECu in 2020 and 2022, respectively. It should be noted that the satellite and receiver DCB correction from the CAS center are applied in the process of extracting the VTEC from GNSS observations of GNSS monitoring stations, which probably affect the accuracy assessment of GIMs. When CAS products are excluded, the smallest value of RMS and bias is found in the COD and ESA, respectively, during the mid-solar and low-solar years. According to the results, it can also be found that the errors of different GIMs with values extracted from the GNSS monitoring station can be divided into two groups. The error indexes of three GIMs, including the EMR, JPL, and UPC, are higher compared to four other GIMs. In terms of the STD, the CAS has the best consistency due to the above-mentioned reasons, and the ESA has the worst consistency with GNSS monitoring stations. The STD values for other GIMs range from 1.555 TECu to 1.638 TECu in 2020 and 2.159 TECu to 2.388 TECu in 2022, which can be found to be in a similar consistency.

Meanwhile, in order to more clearly demonstrate the distribution of errors with GNSS real measurements in different latitude bands, Figures 10 and 11 show the distribution of VTEC differences at the GNSS monitoring sites used in 2020 and 2022. Table 6 shows the RMS values in different latitude bands. It can be seen that the accuracy of the different GIMs is different in each latitude band compared to the GNSS real measurements. Both in low-solar and mid-solar activity years, it remains the case that the accuracy is the worst in the low-latitude band and the highest in the high-latitude band. The RMS values at high, mid, and low latitudes of the Northern and Southern Hemispheres are 2.837 TECu, 2.977 TECu, and 4.517 TECu and 2.434 TECu, 2.673 TECu, and 5.056 TECu, respectively. Overall, the accuracy in the Northern Hemisphere is slightly higher than in the southern hemisphere, with RMS values of 3.388 TECu and 3.444 TECu, respectively, which is mainly because there are more GNSS monitoring stations in the Northern Hemisphere than in the southern hemisphere. The accuracy assessment results of different solar activity years show variations in different latitude bands. According to the results, it is obvious that the ESA is significantly affected by solar activity in the high-latitude band and the low-latitude band,

with differences of 1.109 TECu and 2.837 TECu. The mid-latitude band is hardly affected by solar activity, with the range of difference basically ranging from 0.1 TECu to 0.9 TECu. In the low-latitude band, UPC is least affected. In the high-latitude band of the northern hemisphere, the COD is least affected, while the JPL is the least affected in the high-latitude band of the southern hemisphere. When excluding the effect of the solar activity level, the JPL has the worst accuracy in all the different latitude bands, and is far worse than several other products. The accuracy of the CAS should be the highest globally, but the results show that the COD accuracy is higher than the CAS in the mid- and low-latitude bands of the Southern Hemisphere. After excluding the CAS, WHU has the highest accuracy in both the high-latitude bands of the Southern and Northern Hemispheres, with the EMR having the highest accuracy in the mid- and low-latitude bands of the northern hemisphere.

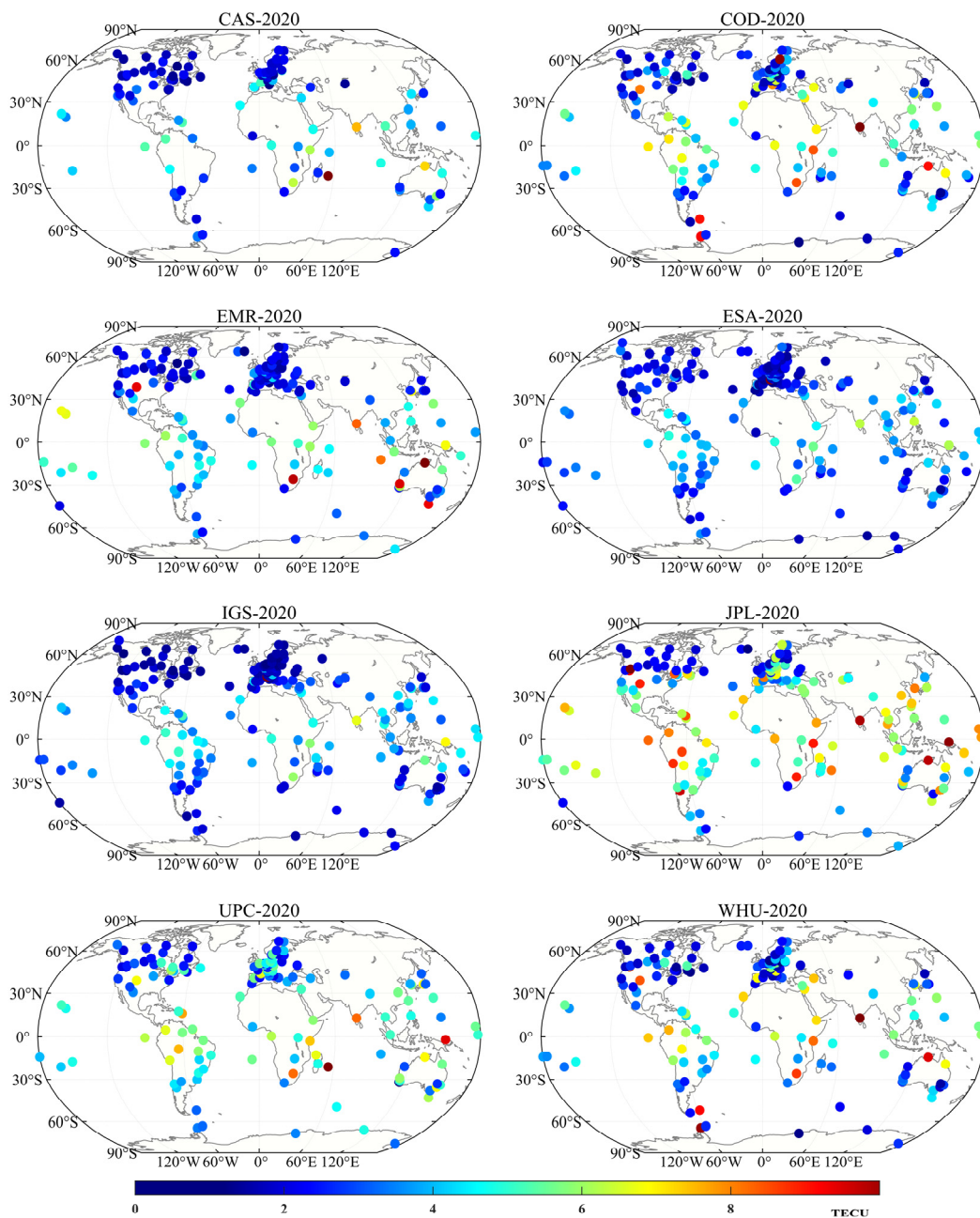


Figure 10. Global distribution of the mean RMS for different GIM products with measured VTEC values in 2020.

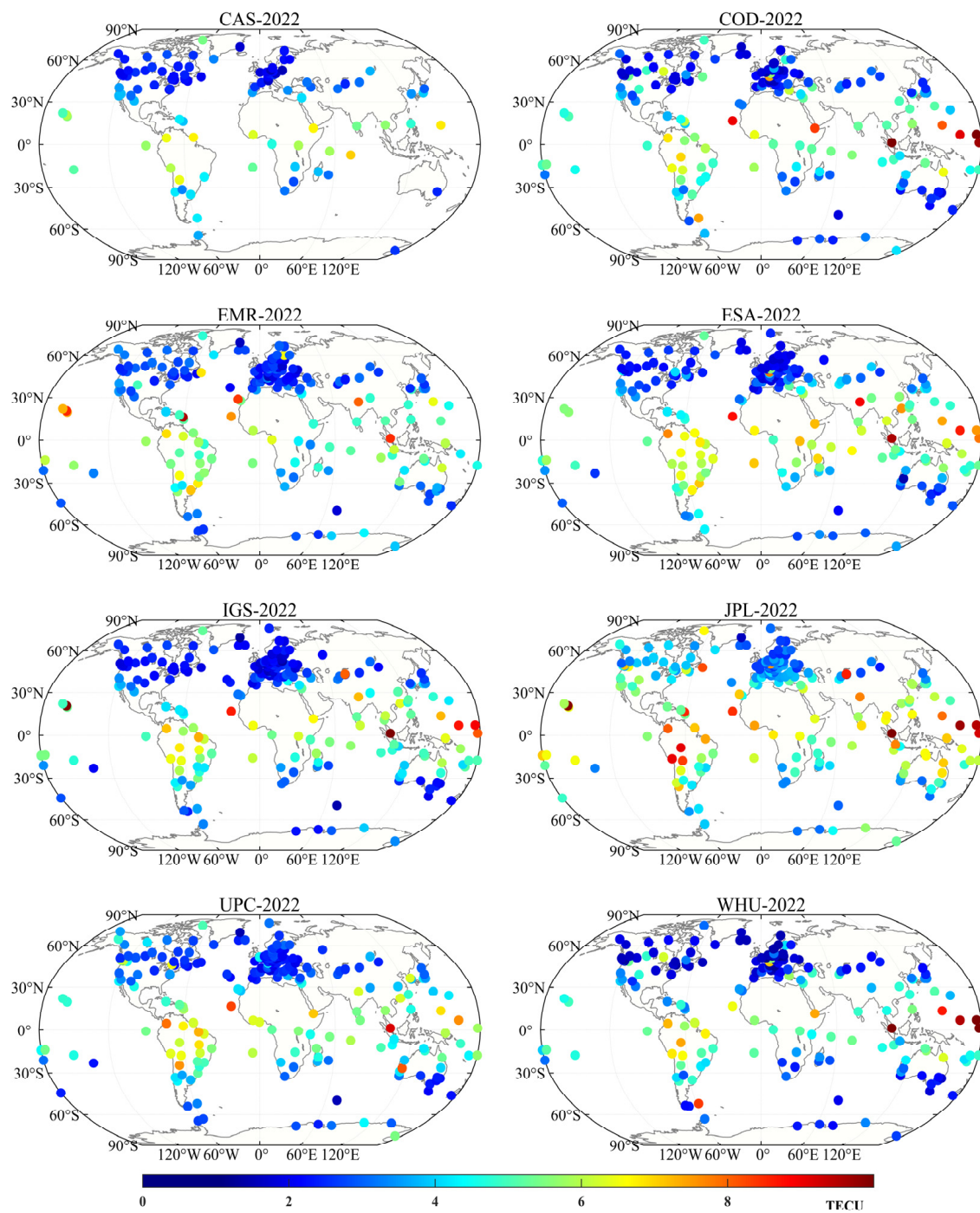


Figure 11. Global distribution of mean RMS for different GIM products with measured VTEC values in 2022.

Table 6. RMS values of different GIMs with GNSS monitoring stations using VTEC in different latitude bands, in the units of TECu.

Latitude	Year	CAS-STA	COD-STA	EMR-STA	ESA-STA	JPL-STA	UPC-STA	WHU-STA
N-H	2020	1.846	2.279	1.942	2.270	2.416	2.072	2.062
	2022	2.506	2.489	3.168	2.483	3.318	2.894	2.337
N-M	2020	2.064	2.146	2.002	2.422	3.532	2.802	2.495
	2022	2.332	2.514	2.537	3.173	3.601	3.402	2.803

Table 6. Cont.

Latitude	Year	CAS-STA	COD-STA	EMR-STA	ESA-STA	JPL-STA	UPC-STA	WHU-STA
N-L	2020	3.747	3.617	3.064	4.012	5.209	4.258	3.690
	2022	5.529	6.280	6.267	5.804	7.571	5.735	6.006
S-L	2020	3.989	3.177	3.291	3.615	4.821	4.434	3.330
	2022	4.928	4.336	5.762	5.610	6.240	4.894	4.805
S-M	2020	2.729	2.479	2.688	2.621	3.666	3.077	2.655
	2022	3.634	2.599	3.134	2.969	4.039	3.202	3.190
S-H	2020	2.234	2.403	2.282	2.286	2.799	2.517	2.578
	2022	2.946	3.114	3.273	3.207	3.279	3.093	2.963

4. Discussion

In this paper, the final GIMs from seven IGS IAACs, including the CAS, COD, EMR, ESA, JPL, UPC, and WHU, are comprehensively evaluated using IGS final GIMs, ionospheric TEC extracted from 243 GNSS monitoring stations, and ionospheric TEC from Jason-3 altimeter satellite as references. The experimental results show that:

- (1) The accuracy of GIMs is worse in the middle years of solar activity than in the low years of solar activity, and is also worse in the low latitudes than in the high latitudes. In general, the accuracy of the JPL is worse in all three experiments, and the average value of VTEC differences can be found to be related to the modeling methods of different GIMs.
- (2) In comparison with the IGS final GIM, the bias of different GIMs is all between 0–2 TECu. As the processing strategies of different GIMs are improving, the numbers of stations and satellites selected are increasing, so the differences between GIMs will gradually become less.
- (3) In comparison with the Jason-3 satellite-based solution, the accuracy of several GIMs is almost the same, except the JPL, with an overall bias between 2–6 TECu. Besides the ionospheric height being higher than the altimeter satellite height, the bias of different GIMs with the Jason-3 satellite is mainly generated based on the data of the GNSS stations distributed on land, where GIMs above ocean are obtained by the spherical harmonic function model or interpolation. So, the accuracy results of different agencies are closely linked with the modeling methods, which demonstrate that the model accuracy of EMR and JPL is overall worse than other GIMs.
- (4) In comparison with the VTEC from GNSS monitoring stations, the mean RMS values of all stations are basically in the range of 0–10 TECu. The accuracy of the JPL is the worst and ESA is most affected by solar activity. Since the DCB products are provided by the CAS center, the accuracy of the CAS is the best in the assessment in experiment. Therefore, when using GIMs for correction, the by-product DCB products of the GIM agency can be adopted to calibrate the correction.

5. Conclusions

In this study, we use the IGS final GIM, ionospheric TEC from 243 GNSS monitoring stations, and ionospheric TEC from the Jason-3 altimeter satellite to evaluate the accuracy and consistency of the global ionospheric grid final product from seven IGS IAACs, including the CAS, COD, EMR, ESA, JPL, UPC, and WHU in mid-solar activity years and low-solar activity years. A comparison with the final GIMs of IGS shows that the differences between each GIM and IGS become smaller as the number of stations increases. Validation with the Jason-3 altimeter satellite shows that the JPL has the largest systematic bias, while the highest accuracy is found from the ESA in low solar activity years and the highest accuracy from the CAS in mid solar activity years. A comparison with VTEC from GNSS monitoring stations shows that the performance of the CAS is the best, but there is a link with DCB. In addition, it can be found that in different latitude bands, the accuracy of

areas with more data is better than that of areas with less data, and it is also closely related to the modeling methods of different GIMs and the DCB products used.

Author Contributions: Conceptualization, W.L.; software, K.W. and K.Y.; validation, W.L. and K.W.; writing—original draft preparation, W.L. and K.W.; writing—review and editing, W.L. and K.Y. All authors have read and agreed to the published version of the manuscript.

Funding: This research was supported by the National Natural Science Foundation of China (grant no. 41804033); and the Open Foundation of Teaching Laboratory of China University of Geosciences (Wuhan) (grant No. SKJ2022196).

Data Availability Statement: All the data presented in this study are openly available in IGS at <https://cddis.nasa.gov/archive/gnss/data/> (accessed on 1 October 2022) and NOAA at <https://www.ncei.noaa.gov/data/oceans/> (accessed on 1 October 2022).

Acknowledgments: The authors would like to thank IGS for providing GNSS datasets and NOAA for providing altimetry datasets, which allowed this study to be completed. All this support is gratefully acknowledged.

Conflicts of Interest: The authors declare no conflict of interest.

References

1. Klobuchar, J.A. Ionospheric Time-Delay Algorithm for Single-Frequency GPS Users. *IEEE Trans. Aerosp. Electron. Syst.* **1987**, *23*, 325–331. [[CrossRef](#)]
2. Hernández-Pajares, M.; Juan, J.M.; Sanz, J.; Orus, R.; Garcia-Rigo, A.; Feltens, J.; Komjathy, A.; Schaer, S.C.; Krankowski, A. The IGS VTEC maps: A reliable source of ionospheric information since 1998. *J. Geod.* **2009**, *83*, 263–275. [[CrossRef](#)]
3. Feltens, J.; Schaer, S.S. IGS Products for the Ionosphere. In Proceedings of the IGS AC Workshop, Darmstadt, Germany, 9–11 February 1998.
4. Feltens, J. The activities of the Ionosphere Working Group of the International GPS Service (IGS). *GPS Solut.* **2003**, *7*, 41–46. [[CrossRef](#)]
5. Schaer, S. *Mapping and Predicting the Earth's Ionosphere Using the Global Positioning System*; Schweizerische Geodätische Kommission: Zürich, Switzerland, 1999; Volume 59.
6. Hernandez-Pajares, M.; Juan, J.M.; Sanz, J. New approaches in global ionospheric determination using ground GPS data. *J. Atmos. Sol.-Terr. Phys.* **1999**, *61*, 1237–1247. [[CrossRef](#)]
7. Mannucci, A.J.; Wilson, B.D.; Yuan, D.N.; Ho, C.H.; Lindqwister, U.J.; Runge, T.F. A global mapping technique for GPS-derived ionospheric total electron content measurements. *Radio Sci.* **1998**, *33*, 565–582. [[CrossRef](#)]
8. Komjathy, A.; Sparks, L.; Wilson, B.D.; Mannucci, A.J. Automated daily processing of more than 1000 ground-based GPS receivers for studying intense ionospheric storms. *Radio Sci.* **2005**, *40*, 1–11. [[CrossRef](#)]
9. Feltens, J.; Dow, J. Realized and planned improvements in ESA/ESOC ionosphere modelling. In Proceedings of the IGS Workshop, Darmstadt, Germany, 8–12 May 2006.
10. Hernandez-Pajares, M. *IGS Ionosphere WG Status Report: Performance of IGS Ionosphere TEC Maps*; IGS Workshop: Bern, Switzerland, 2004; pp. 225–237.
11. Schaer, S.; Gurtner, W.; Feltens, J. IONEX: The ionosphere map exchange format version 1. In Proceedings of the IGS AC Workshop, Darmstadt, Germany, 9–11 February 1998.
12. Peng, C.; Chen, J. Analysis of factors affecting accuracy of global ionospheric grid model. *J. Geod. Geodyn.* **2014**, *34*, 105–114. [[CrossRef](#)]
13. Zhang, Q.; Zhao, Q.L. Evaluation and analysis of the global ionosphere maps from Wuhan University IGS Ionosphere Associate Analysis Center. *Chin. J. Geophys.-Chin. Ed.* **2019**, *62*, 4493–4505. [[CrossRef](#)]
14. Li, Z.; Yuan, Y.; Li, H.; Ou, J.; Huo, X. Two-step method for the determination of the differential code biases of COMPASS satellites. *J. Geod.* **2012**, *86*, 1059–1076. [[CrossRef](#)]
15. Zhang, B.C.; Teunissen, P.J.G.; Yuan, Y.B.; Zhang, H.X.; Li, M. Joint estimation of vertical total electron content (VTEC) and satellite differential code biases (SDCBs) using low-cost receivers. *J. Geod.* **2018**, *92*, 401–413. [[CrossRef](#)]
16. Dow, J.M.; Neilan, R.E.; Rizos, C. The International GNSS Service in a changing landscape of Global Navigation Satellite Systems. *J. Geod.* **2009**, *83*, 191–198. [[CrossRef](#)]
17. Zhang, B.C.; Teunissen, P.J.G.; Yuan, Y.B.; Zhang, X.; Li, M. A modified carrier-to-code leveling method for retrieving ionospheric observables and detecting short-term temporal variability of receiver differential code biases. *J. Geod.* **2019**, *93*, 19–28. [[CrossRef](#)]
18. Jee, G.; Lee, H.B.; Kim, Y.H.; Chung, J.K.; Cho, J. Assessment of GPS global ionosphere maps (GIM) by comparison between CODE GIM and TOPEX/Jason TEC data: Ionospheric perspective. *J. Geophys. Res. Space Phys.* **2010**, *115*. [[CrossRef](#)]
19. Zhang, B.C.; Ou, J.K.; Yuan, Y.B.; Li, Z.S. Extraction of line-of-sight ionospheric observables from GPS data using precise point positioning. *Sci. China-Earth Sci.* **2012**, *55*, 1919–1928. [[CrossRef](#)]

20. Chen, P.; Yao, Y.B.; Yao, W.Q. Global ionosphere maps based on GNSS, satellite altimetry, radio occultation and DORIS. *GPS Solut.* **2017**, *21*, 639–650. [[CrossRef](#)]
21. Ho, C.M.; Wilson, B.D.; Mannucci, A.J.; Lindqwister, U.J.; Yuan, D.N. A comparative study of ionospheric total electron content measurements using global ionospheric maps of GPS, TOPEX radar, and the Bent model. *Radio Sci.* **1997**, *32*, 1499–1512. [[CrossRef](#)]
22. Orús, R.; Hernández-Pajares, M.; Juan, J.M.; Sanz, J.; García-Fernández, M. Performance of different TEC models to provide GPS ionospheric corrections. *J. Atmos. Sol.-Terr. Phys.* **2002**, *64*, 2055–2062. [[CrossRef](#)]
23. Roma-Dollase, D.; Hernandez-Pajares, M.; Krankowski, A.; Kotulak, K.; Ghoddousi-Fard, R.; Yuan, Y.B.; Li, Z.S.; Zhang, H.P.; Shi, C.; Wang, C.; et al. Consistency of seven different GNSS global ionospheric mapping techniques during one solar cycle. *J. Geod.* **2018**, *92*, 691–706. [[CrossRef](#)]
24. Luo, W.; Liu, Z.; Li, M. A preliminary evaluation of the performance of multiple ionospheric models in low- and mid-latitude regions of China in 2010–2011. *GPS Solut.* **2013**, *18*, 297–308. [[CrossRef](#)]
25. Nie, Z.X.; Yang, H.Z.; Zhou, P.Y.; Gao, Y.; Wang, Z.J. Quality assessment of CNES real-time ionospheric products. *GPS Solut.* **2019**, *23*, 11. [[CrossRef](#)]
26. Jerez, G.O.; Hernandez-Pajares, M.; Prol, F.S.; Alves, D.B.M.; Monico, J.F.G. Assessment of Global Ionospheric Maps Performance by Means of Ionosonde Data. *Remote Sens.* **2020**, *12*, 3452. [[CrossRef](#)]
27. Li, Z.S.; Wang, N.B.; Li, M.; Zhou, K.; Yuan, Y.B.; Yuan, H. Evaluation and analysis of the global ionospheric TEC map in the frame of international GNSS services. *Chin. J. Geophys.-Chin. Ed.* **2017**, *60*, 3718–3729. [[CrossRef](#)]
28. Zhang, M.-L.; Radicella, S.M.; Shi, J.-K.; Wang, X.; Wu, S.-Z. Comparison among IRI, GPS-IGS and ionogram-derived total electron contents. *Adv. Space Res.* **2006**, *37*, 972–977. [[CrossRef](#)]
29. Xue, J.C.; Song, S.L.; Zhu, W.Y. Assessment of CODE GIM over China. In Proceedings of the ION 2013 Pacific PNT Meeting, Honolulu, HI, USA, 23–25 April 2013; pp. 706–722.
30. Yu, L.; Yibin, Y.; Liang, Z. Accuracy Assessment of CODE GIM in China. *J. Geomat.* **2021**, *46*, 8–12. [[CrossRef](#)]
31. Xiang, Y.; Yuan, Y.; Li, Z.; Wang, N. Analysis and validation of different global ionospheric maps (GIMs) over China. *Adv. Space Res.* **2015**, *55*, 199–210. [[CrossRef](#)]
32. Wang, S.; Liu, L.; Huang, L.; Yang, Y.; Peng, H. Performance evaluation of ionospheric tec forecasting models using gps observations at different latitudes. *ISPRS—Int. Arch. Photogramm. Remote Sens. Spat. Inf. Sci.* **2020**, *XLII-3/W10*, 1175–1182. [[CrossRef](#)]
33. Imel, D.A. Evaluation of the topex/poseidon dual-frequency ionosphere correction. *J. Geophys. Res.-Ocean* **1994**, *99*, 24895–24906. [[CrossRef](#)]
34. Ciraolo, L.; Azpilicueta, F.; Brunini, C.; Meza, A.; Radicella, S.M. Calibration errors on experimental slant total electron content (TEC) determined with GPS. *J. Geod.* **2007**, *81*, 111–120. [[CrossRef](#)]
35. Brunini, C.; Azpilicueta, F. GPS slant total electron content accuracy using the single layer model under different geomagnetic regions and ionospheric conditions. *J. Geod.* **2010**, *84*, 293–304. [[CrossRef](#)]
36. Zhang, B.C.; Teunissen, P.J.G.; Yuan, Y. On the short-term temporal variations of GNSS receiver differential phase biases. *J. Geod.* **2016**, *91*, 563–572. [[CrossRef](#)]
37. Zhang, B.C.; Teunissen, P.J.G. Characterization of multi-GNSS between-receiver differential code biases using zero and short baselines. *Sci. Bull.* **2015**, *60*, 1840–1849. [[CrossRef](#)]

Disclaimer/Publisher’s Note: The statements, opinions and data contained in all publications are solely those of the individual author(s) and contributor(s) and not of MDPI and/or the editor(s). MDPI and/or the editor(s) disclaim responsibility for any injury to people or property resulting from any ideas, methods, instructions or products referred to in the content.